ADVANCED MATERIALS
www.advmat.de

Room-Temperature Gate-Tunable Nonreciprocal Charge Transport in Lattice-Matched InSb/CdTe Heterostructures

Lun Li, Yuyang Wu, Xiaoyang Liu, Jiuming Liu, Hanzhi Ruan, Zhenghang Zhi, Yong Zhang, Puyang Huang, Yuchen Ji, Chenjia Tang, Yumeng Yang, Renchao Che, and Xufeng Kou**

Symmetry manipulation can be used to effectively tailor the physical order in solid-state systems. With the breaking of both the inversion and time-reversal symmetries, nonreciprocal magneto-transport may arise in nonmagnetic systems to enrich spin–orbit effects. Here, the observation of unidirectional magnetoresistance (UMR) in lattice-matched InSb/CdTe films is investigated up to room temperature. Benefiting from the strong built-in electric field of 0.13 V nm^{-1} in the heterojunction region, the resulting Rashba-type spin–orbit coupling and quantum confinement result in a distinct sinusoidal UMR signal with a nonreciprocal coefficient that is 1–2 orders of magnitude larger than most non-centrosymmetric materials at 298 K. Moreover, this heterostructure configuration enables highly efficient gate tuning of the rectification response, wherein the UMR amplitude is enhanced by 40%. The results of this study advocate the use of narrow-bandgap semiconductor-based hybrid systems with robust spin textures as suitable platforms for the pursuit of controllable chiral spin–orbit applications.

1. Introduction

Symmetry, which lies at the heart of universal laws, serves as a fundamental degree of freedom for defining the intrinsic properties of a material.[1] Coupled with spin–orbit coupling (SOC), the breaking of inversion symmetry modifies the Hamiltonian of charge carriers with antisymmetric momentum operators, resulting in nonreciprocal transport phenomena featuring unidirectional I–V characteristics.[2] To realize such a rectification effect, the magnetochiral anisotropy originating from either non-centrosymmetric band structures or heterointerfaces is required.[3–5] The inherent bulk/interfacial Rashba-type SOC lifts the spin degeneracy and triggers current-induced spin polarization.[6–12] Through the further application of an external magnetic field to break the time-reversal symmetry, the regulation of the asymmetric spin splitting can be represented by the nonreciprocal electrical response. In this case, the longitudinal resistance exhibits a unique current-direction-dependent signature and its second-order harmonic component scales linearly with both the applied current and the magnetic field.[2,4,5,12–16] Governed by the spin–momentum locking mechanism, this unidirectional magnetoresistance (UMR) can be established without invoking additional magnetic order, thereby unfolding a reliable approach for exploring the spin–orbit dynamics in a variety of low-crystalline symmetry systems, including topological insulators/semimetals (e.g., Bi_2Se_3[17] and WTe_2[18]), polar semiconductors (e.g., BiTeBr,[5] α-GeTe,[19] and Te[20]), and heterostructures (e.g., $LaAlO_3/SrTiO_3$[4] and Ge/Si[21]).

The amplitude of the Rashba-type UMR signal is closely linked to the spin splitting energy $\Delta\varepsilon \sim \alpha_R \cdot (\Delta k \times \hat{n}) \cdot \sigma$ (where

L. Li, X. Liu, J. Liu, H. Ruan, Z. Zhi, Y. Zhang, P. Huang, Y. Yang, X. Kou
School of Information Science and Technology
ShanghaiTech University
Shanghai 201210, China
E-mail: kouxf@shanghaitech.edu.cn

Y. Wu, R. Che
Laboratory of Advanced Materials
Shanghai Key Lab of Molecular Catalysis and Innovative Materials
Fudan University
Shanghai 200438, China
E-mail: rcche@fudan.edu.cn

Y. Wu, R. Che
Department of Materials Science
Fudan University
Shanghai 200438, China

The ORCID identification number(s) for the author(s) of this article can be found under https://doi.org/10.1002/adma.202207322.

X. Liu, Z. Zhi, Y. Zhang
Shanghai Institute of Microsystem and Information Technology
Chinese Academy of Sciences
Shanghai 200050, China

X. Liu, Z. Zhi, Y. Zhang
University of Chinese Academy of Science
Beijing 101408, China

Y. Ji, C. Tang
School of Physical Science and Technology
ShanghaiTech University
Shanghai 201210, China

C. Tang, X. Kou
ShanghaiTech Laboratory for Topological Physics
ShanghaiTech University
Shanghai 201210, China

DOI: 10.1002/adma.202207322

α_R is the Rashba coefficient, **k** is the momentum vectors, $\boldsymbol{\sigma}$ is the Pauli operator, and the mirror symmetry is broken along the $\hat{n}$ direction), the spin relaxation time τ, and the Fermi energy ε_F, which is the key to facilitating the aforementioned nonreciprocal charge transport that relies on the optimization of the internal polarization/electrical field as well as the Fermi level position.[4,5,19] Accordingly, with appropriate heterostructure integration, the band bending at the interface facilitates the introduction of a built-in electric field that ensures strong Rashba-type spin–orbit interaction. Further, the well-developed quantum well aids in confining the electron conduction within the 2D channel (i.e., secures a long phase-coherent/scattering length). In addition, such band engineering enables the direct modulation of the Rashba SOC strength and Fermi level through the gate bias, which may cultivate versatile voltage-controlled nonreciprocal functionalities.

Inspired by the above design rules, this study demonstrated the use of InSb/CdTe heterostructures to achieve electric-field control of nonreciprocal charge transport up to room temperature. As illustrated in **Figure 1**a, the integration of the narrow-bandgap InSb thin film and the wide-bandgap CdTe buffer layer exploits the type-I heterojunction with a large conduction-band offset (ΔE_C = 0.31 eV) to generate a strong built-in electric field and Rashba coefficient; both these values are the highest among reported III–V semiconductor-based heterostructures. Moreover, the identical lattice constants between two adjacent layers guarantee the formation of an atomically sharp interface that ensures spin-polarized electron conduction. Consequently, the giant Rashba field-induced spin splitting energy of the InSb/CdTe system results in enhanced unidirectional magnetoresistance and a gate-tunable nonreciprocal coefficient γ over the entire temperature range of 1.5 K < T < 298 K. These observations highlight the importance of heterostructure engineering in preserving the nonreciprocal responses at room temperature. Moreover, they offer feasible strategies for energy-efficient spin-state manipulation.

2. Result and Discussion

2.1. Giant Built-In Electric Field in InSb/CdTe Heterostructures

High-quality InSb/CdTe thin films were grown on a 3 in. semi-insulating GaAs(111)B wafer via molecular beam epitaxy

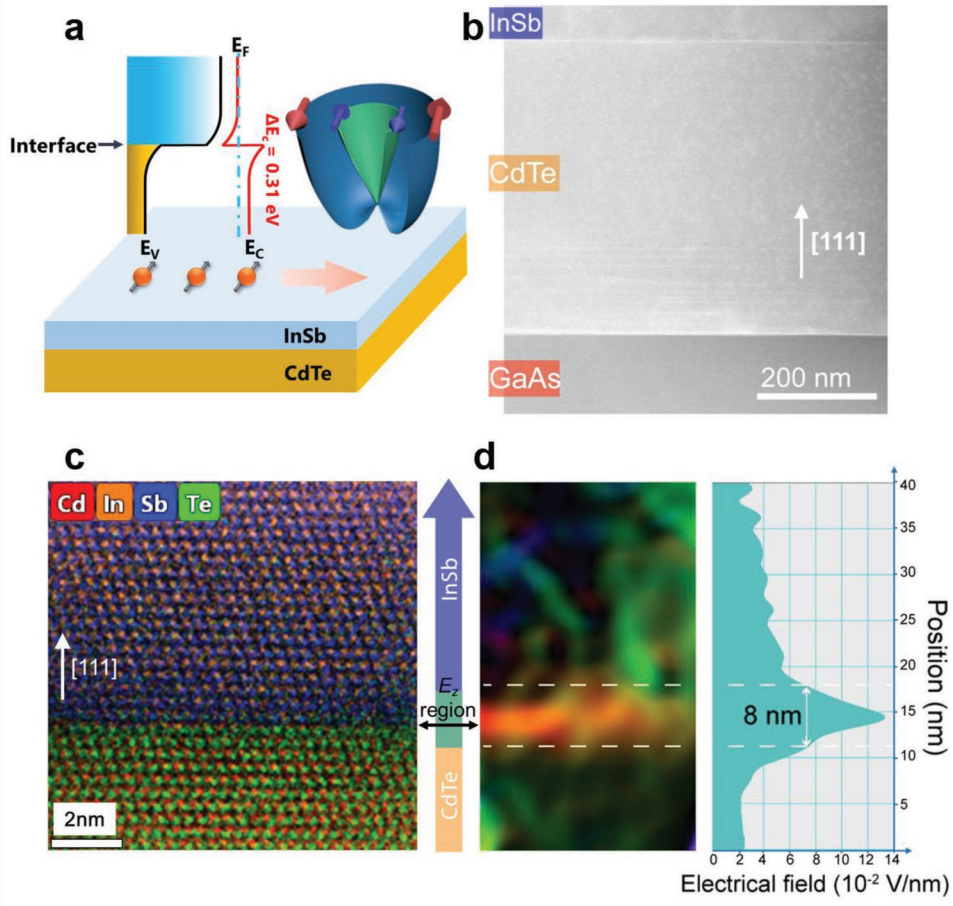

Figure 1. Structural characterizations of the InSb (30 nm)/CdTe (400 nm) heterostructures. a) Schematic of the InSb/CdTe heterostructure and relevant energy band diagram. The well-established band bending at the InSb/CdTe heterojunction causes a strong Rashba-type spin–orbit coupling on the spin sub-bands and forces the interfacial electrons to spin-polarize perpendicular to the current direction. b) Cross-sectional HAADF image shows the intact interface of the InSb/CdTe sample. c) Atomic-resolution EDS mapping near the InSb/CdTe interface region. d) Electron holography profile confirms the existence of a strong built-in electric-field region with the peak intensity of 0.13 V nm^{-1} and the average width of 8 nm.

(MBE).[22] Detailed growth information and sample characterizations are provided in Section S1 (Supporting Information). Figure 1b shows the cross-sectional high-angle annular dark-field (HAADF) profile of the as-grown sample, which confirms the absence of macroscopic threading dislocations in the examined region. The structural characteristics near the InSb/CdTe junction were visualized via atomic-resolution X-ray energy-dispersive spectroscopy (EDS) mapping (Figure 1c). As evident, all the In, Sb, Cd, and Te atoms rigorously followed the zinc blende configuration along the [111] direction, and the defect-free heterointerface was well-defined with negligible intermixing among the constituent elements. This validates the epitaxial growth of the single-crystalline heterostructures. Furthermore, the built-in electric field owing to interfacial band bending was quantified through off-axis electron holography. Owing to the nonmagnetic property of the InSb/CdTe sample, the phase shift of the incident electron beam was only affected by the electric-field signal inside the sample. Therefore, the distribution of the internal electric potential was obtained from the relevant phase diagram (Figure S2, Supporting Information).[23] As shown in Figure 1d, the peak position of the electric field was located at the InSb/CdTe interface, and its corresponding maximum intensity (E_{max} = 0.13 V nm^{-1} at T = 298 K) was much higher than both the conventional GaAs/$Al_xGa_{1-x}As$ quantum wells (0.015–0.045 V nm^{-1}) and the InAs/GaSb superlattice (0.08 V nm^{-1}).[24] Moreover, the full width at half maximum of the electric-field spectrum was ≈8 nm, and the electric potential energy difference of 0.3 eV was obtained by integrating the electric field within the heterojunction region. These results are consistent with the band diagram simulated by technology computer-aided design (TCAD),[25] thereby further validating the existence of the giant Rashba effect in the lattice-matched InSb/CdTe system.

2.2. Room-Temperature Rashba-Type Unidirectional Magnetoresistance

In our previous study, we detected distinct spin–torque ferromagnetic resonance (ST-FMR) signals from hybrid Py-InSb/CdTe films at T = 298 K,[26] which suggests productive spin polarization in the InSb/CdTe channel up to room temperature. To further investigate the inversion-asymmetry-related effects, angular-dependent magneto-transport measurements were performed on a micrometer-size six-probe Hall bar device patterned from the MBE-grown InSb (30 nm)/CdTe (400 nm) sample (see the "Experimental Section"). As the interfacial Rashba SOC-induced pseudomagnetic field B_{eff} is tightly locked to the product of the momentum operator and built-in electric field (i.e., $B_{eff} = \alpha_R \cdot (k_x \times \hat{z})$), it influences the in-plane spin-dependent scattering. Consequently, via the application of a low-frequency AC current $I = I_0 \sin(\omega t)$ along the $+x$ direction while rotating the external magnetic field in the xy-plane (i.e., the angle between **B** and I is defined as ϕ), the second-harmonic components of both the longitudinal ($V_{xx}^{2\omega}$) and vertical ($V_{xy}^{2\omega}$) voltages were recorded using the standard lock-in technique. **Figure 2**a shows one set of nonlinear resistance pairs ($R_{xx}^{2\omega} = V_{xx}^{2\omega}/I_0$, $R_{xy}^{2\omega} = V_{xy}^{2\omega}/I_0$) under a particular input condition of B = 14 T and I_0 = 400 μA, where two sinusoidal slopes with the same period of 360° but a phase difference of 90° were observed in the $R^{2\omega}$–ϕ diagram at T = 298 K. By excluding the thermal contribution owing to the Nernst effect (i.e., the current-induced vertical temperature gradient also causes a nonlinear transport response; Figure S3, Supporting Information), the Rashba-type UMR behavior is subsequently demonstrated in Figure 2b–d; that is, the extracted second-harmonic magnetoresistance $R_{UMR}^{2\omega}$ reaches its highest (lowest) state at ϕ = 90° (270°), whereas it vanishes when ϕ = 0° and 360° (i.e., the sinϕ-shape UMR response is further confirmed by DC measurement, as discussed in Section S4 of the Supporting Information). Similar to other non-centrosymmetric materials, the UMR amplitude $\Delta R_{UMR}^{2\omega}$ in our InSb/CdTe sample also exhibited a linear relationship with the magnetic field (up to 14 T) and the charge current (up to 600 μA), thereby manifesting the $\Delta R_{UMR}^{2\omega} \propto BI_0$ nature of nonreciprocal transport.[4,5,21]

To understand the interplay between the Rashba-type spin splitting and $\Delta R_{UMR}^{2\omega}(\phi, B)$, first recall that the Fermi level position within the InSb/CdTe junction region resides above the conduction band Γ_6 of InSb (see Figure S5 in the Supporting Information).[25,27] Through the application of a current along the $+x$-axis, the interfacial conducting electrons are spin-polarized toward the $+y$ direction, and the 2D Rashba Hamiltonian under an in-plane magnetic field is expressed as

$$H = \frac{\hbar(k_x^2 + k_y^2)}{2m^*} + (\alpha_R k_x)\sigma_y - \left(\frac{1}{2} g\mu_B B \sin\phi\right)\sigma_y \quad (1)$$

where ħ is the reduced Planck constant, $m^* = 0.03m_e$ is the electron effective mass of InSb,[28] g = −42 is the in-plane g-factor,[29,30] μ_B is the Bohr magneton, and the Rashba coefficient α_R = 0.4 eV Å is deduced from the weak antilocalization data.[31] Considering this database, a semiempirical energy band dispersion with $|\alpha_R k_F|$ = 9 meV and $\Delta\varepsilon_z = g\mu_B B$ = −34 meV in the presence of B = 14 T is shown in the top panel of Figure 2e. Based on the nonlinear second-order spin–orbit-coupled magneto-transport model, the Δk-induced spin sub-band displacement tilts the electron distribution at the Fermi surface, and the in-plane magnetic field disequilibrates the spin-up and spin-down densities in the system.[17,19,21] Accordingly, the second-order variation of the electron distribution δf_2 results in a nonzero second-order charge current $J_c' \propto E_x^2 \cdot B\sin\phi \propto \Delta R_{UMR}^{2\omega}$.[5,17,19] As shown in the bottom panel of Figure 2e, the $(+B_y, +E_x)$ condition initiates a majority of electrons with a $+\sigma_y$ spin state, which then drives the induced $J_c'(+B_y, +E_x^2)$ along the $-x$ direction; in contrast, the reversal of the applied magnetic field to $-B_y$ switches the sign of $J_c'(-B_y, +E_x^2)$ toward the $+x$ direction. Consequently, a high (low)-resistance state is expected when the magnetic field is parallel (antiparallel) to the spin-polarization direction, which is consistent with the UMR results shown in Figure 2b. Moreover, $\Delta R_{UMR}^{2\omega}$ evolves nonmonotonously from T = 1.5 to 298 K (inset of Figure 2b), which may correlate with the temperature-dependent density of states at the Fermi surface.[19] However, quantitative electronic band structure calculations of InSb in the presence of Rashba splitting under external fields are required for future studies.

Based on the same principle discussed earlier, we can map the spin texture of the InSb/CdTe heterostructures by tracing the nonreciprocal transport signal with respect to the current

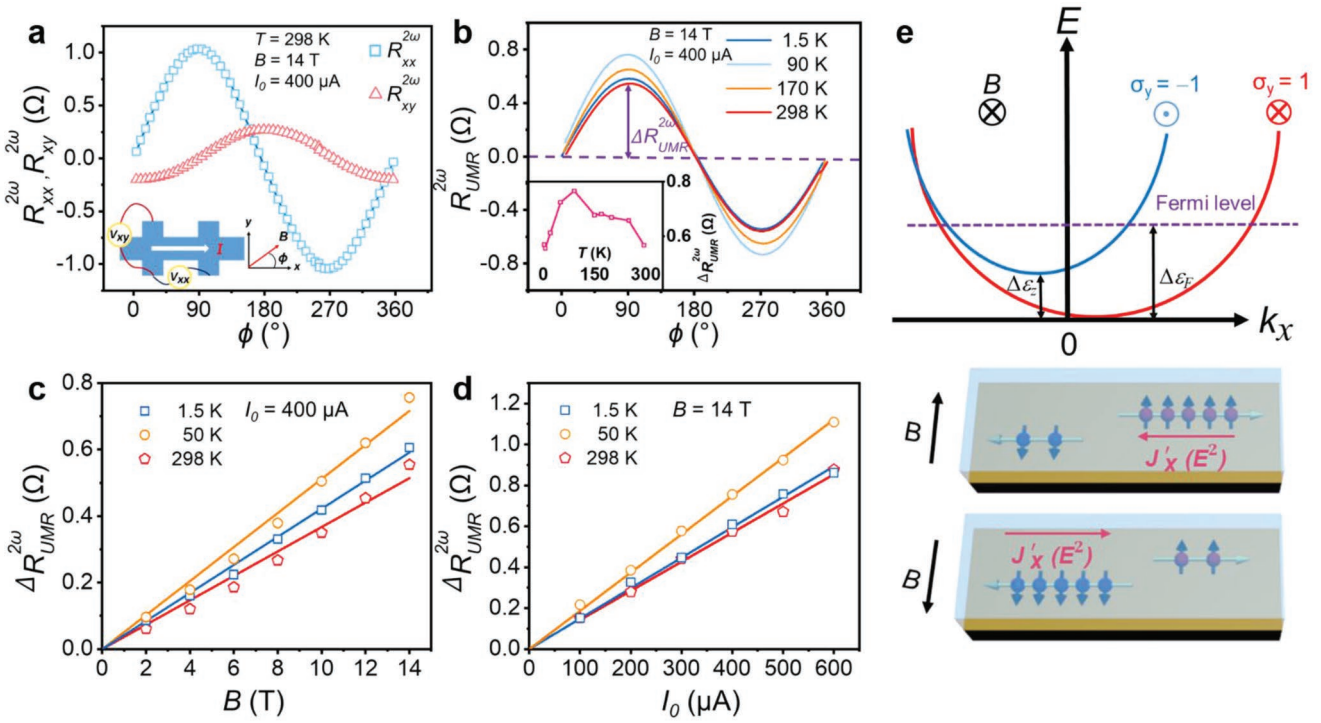

Figure 2. Rashba-type unidirectional magnetoresistance effect in the InSb/CdTe heterostructures. a) Angular-dependent second-harmonic longitudinal ($R^{2\omega}_{xx}$) and vertical ($R^{2\omega}_{xy}$) resistances of the InSb (30 nm)/CdTe (400 nm) sample at T = 298 K. Both data were recorded using standard lock-in technique when the applied magnetic field continuously rotates in the xy-plane. The inset image illustrates the measurement setup and the rotation angle definition. b) Rashba spin-splitting-induced sinusoidal UMR component $R^{2\omega}_{UMR}$ probed from 1.5 to 298 K. Inset: the UMR amplitude $\Delta R^{2\omega}_{UMR}$ displays a nonmonotonical dependence on temperature. c) UMR amplitude is proportional to the applied in-plane magnetic field under a fixed current amplitude of I_0 = 400 μA. d) Linear current-dependent $\Delta R^{2\omega}_{UMR}$ curves under the same B = 14 T. e) Band structure of the InSb conduction band with the magnetic field along the +y direction. Owing to the negative g-factor of InSb, the negative Zeeman energy $\Delta\varepsilon_z$ = −34 meV drives the spin-up sub-band (red) below the spin-down sub-band (blue). The Fermi level $\Delta\varepsilon_F$ = 58 meV is located above the conduction-band minimum (CBM), and the cross point of the sub-bands $\Delta\varepsilon_{cp}$ = 209 meV is much higher than CBM. Therefore, the second-order current is enhanced (suppressed) by the in-plane magnetic field parallel (antiparallel) to the spin polarization.

and magnetic field directions. For instance, **Figure 3**a–c shows three UMR slopes measured by rotating B_{yz} = 14 T in the yz-plane, with the angles between the input current and the x-axis being set as ϕ = 90°, 60°, and 30°, respectively. All $R^{2\omega}_{UMR}$ curves exhibited sinusoidal angular dependence with a period of 360°, and the normalized peak amplitude ratio of $\Delta R^{2\omega}_{UMR}(\phi)/\Delta R^{2\omega}_{UMR}(\phi = 90°)$ followed the sinϕ relation (Figure 3d). Compared with the in-plane reference data recaptured from Figure 2b (red line), we may conclude that the nonreciprocal response in our sample primarily stems from the conduction channel at the heterointerface. Here, the interfacial Rashba spin–orbit interaction only produces spin polarization strictly orthogonal to $\mathbf{k} \times \mathbf{E}_z$ (i.e., a counterclockwise spin chirality of the outer branch in the k-space), and there is no out-of-plane spin component because the $R^{2\omega}_{UMR}$ contours in the xy- and yz-planes are identical to each other (Figure 3a). In addition, we also performed angular-dependent second-order harmonic measurements on several Hall bar devices fabricated along different crystal orientations, and the obtained UMR results disclosed the isotropic feature of the energy band in the xy-plane (see Figure S6 in the Supporting Information).

To evaluate the strength of the nonreciprocal charge transport, we chose the nonreciprocal coefficient $\gamma = 2\Delta R^{2\omega}_{xx}/(BI_0R_0)$ as the main figure of merit. From the summarized temperature-dependent γ data in various non-centrosymmetric systems (Figure 3e), our InSb/CdTe thin film clearly distinguished itself from this benchmark chart in terms of both large γ = 0.52 A^{-1} T^{-1} and robust thermal stability. In particular, guided by the criteria of $\gamma \propto g\alpha_R\tau^2/\varepsilon_F$, it is evident that although polar semimetals and semiconductors (e.g., WTe_2,[18] α-GeTe,[19] and Bi-helix[32]) inherit giant bulk Rashba coefficients as high as 2–5 eV Å, the metallic electrical properties (i.e., high carrier density and bulk scattering) inevitably limit the magnitude of γ below 10^{-2} A^{-1} T^{-1} at room temperature. On the other hand, although semiconductor and oxide heterostructures (e.g., SiO_2/Si,[33] Ge/Si,[21] and $LaAlO_3/SrTiO_3$[4]) host 2D electron gas channels at low temperatures, the weak band bending and small spin splitting energy (3–5 meV) render the systems vulnerable to thermal fluctuations; that is, the UMR signals experience significant attenuation with increasing temperatures and are barely observable at room temperature. Consequently, the combination of a strong interfacial Rashba SOC, high electron mobility (μ_e = 2800 cm^2 V^{-1} s^{-1}; see Figure S7a in the Supporting Information), relatively small Fermi energy (ε_F = 58 meV), and temperature stability endowed the lattice-matched InSb/CdTe system with an optimized γ value over the entire temperature range.

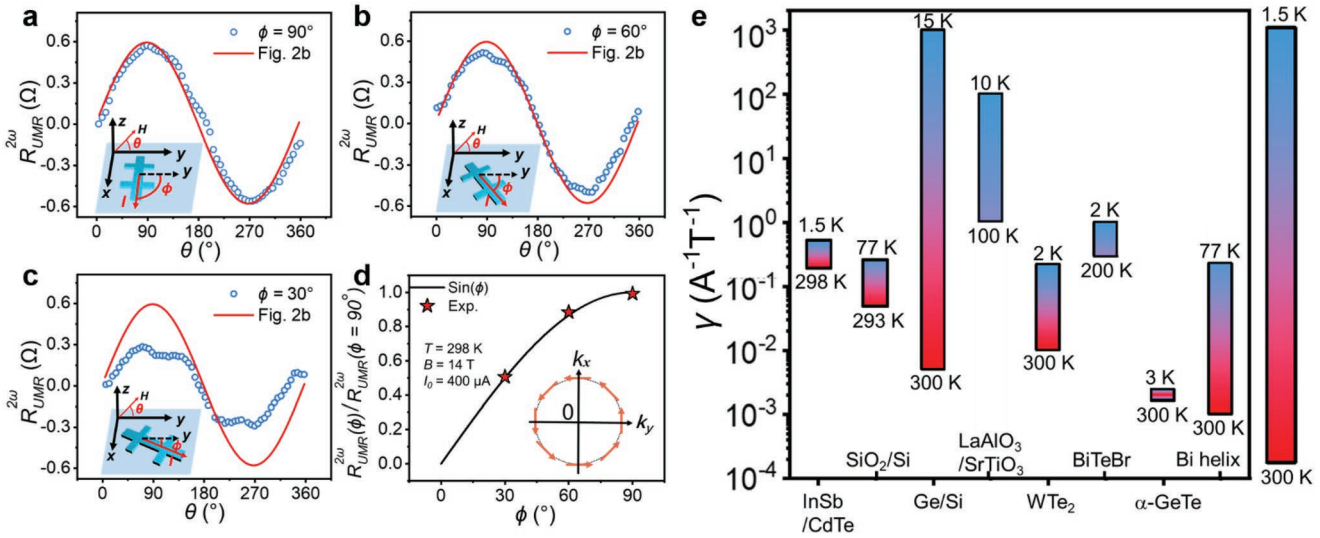

Figure 3. Mapping nonreciprocal transport responses in the InSb/CdTe heterostructures. a–c) Angular-dependent UMR results of the InSb (30 nm)/CdTe (400 nm) sample at $T = 298$ K. The applied magnetic field rotates within the *yz*-plane while the angles between input current and the *x*-axis are chosen as $\phi = 90°$, 60°, and 30°, as shown in the inset schematics. d) The normalized UMR amplitude can be depicted by the rigorous $\sin\phi$ relation, indicating the absence of any out-of-plane spin-polarization component. Inset: Counterclockwise spin chirality of the interfacial electrons in the *k*-space. e) Comparison of the nonreciprocal coefficient in various non-centrosymmetric material systems. Our InSb/CdTe sample stands out from the category by exhibiting a thermal-stable nonreciprocal coefficient with a large γ-value at room temperature.

2.3. Electric-Field Control of the Nonreciprocal Transport

Owing to the effective gate tuning of the Rashba SOC strength in the InSb/CdTe heterostructures,[25] we further deposited a 50 nm Al_2O_3 dielectric layer on top of the InSb (30 nm)/CdTe (400 nm) wafer and designed the top-gated Hall bar structure using a nanofabrication process (**Figure 4**a). The gate-dependent UMR results of the fabricated device at $T = 1.5$ K are shown in Figure 4b. By changing the gate voltage (V_G) from −4 to +6 V, the normalized $R^{2\omega}_{norm} = R^{2\omega}_{UMR}(V_G)/\Delta R^{2\omega}_{UMR}(V_G = 0)$ curves all retained the original $\sin\phi$ line shape. Further, the nonreciprocal amplitude $\Delta R^{2\omega}_{UMR}(V_G)$ successively shrank from 0.67 to 0.47 Ω (i.e., 40% gate-voltage modulation efficiency), and the same negatively correlated γ_{norm}–V_G trend can be observed from 1.5 up to 298 K, as shown in Figure 4c.

According to the TCAD-simulated spatial distribution profile of electron density across the Al_2O_3/InSb/CdTe structure (Figure 4d), the top-gate configuration enables effective charge-carrier regulation within the InSb layer owing to its semiconducting nature. Specifically, the applied negative bias introduces several holes (i.e., $Q = C_{ox} \cdot V_G$, where C_{ox} is the capacitance of the Al_2O_3 layer) into the n-type InSb layer, and thereafter drives the Fermi level position toward the InSb bandgap center. Upon depletion near the top Al_2O_3/InSb interface, a majority of the charge current is conducted through the underlying InSb/CdTe interfacial channel with a strong built-in potential. Under such circumstances, both the enhanced Rashba SOC strength[25] and lowered Fermi energy aid in amplifying the nonreciprocal transport response. Moreover, the top depletion region would also leave the band bending near the bottom InSb/CdTe interface less affected by the applied electric field (i.e., the carrier density and mobility of the InSb conduction channel display a weak dependence on the negative gate voltage, as discussed in Section S7 in the Supporting Information). Consequently, the nonreciprocal coefficient γ saturated in the $V_G < 0$ region. In contrast, when $V_G > 0$ V was applied, the induced excessive electrons resulted in the bulk-dominated conduction scenario with a damped γ-value (i.e., the majority of itinerant carriers within the electron accumulation layer near the Al_2O_3/InSb interface would experience suppressed α_R and τ because of a less ideal interface quality). In addition, the increase in temperature promoted thermal activation with a more dominant bulk conduction in the top-gated InSb/CdTe device. Consequently, the gate-voltage modulation was less effective at higher temperatures (Figure 4c). In addition to the UMR effect arising from the second-order charge current, the first-order anisotropic magnetoresistance (AMR) of our InSb/CdTe heterostructures revealed a unique gate-dependent trait. As shown in Figure 4e, the AMR amplitude of the Al_2O_3 (50 nm)/InSb (30 nm)/CdTe (400 nm) device increased significantly with an increase in the applied gate voltage (i.e., corresponding to the transition from InSb/CdTe heterojunction conduction to bulk InSb transport). Concurrently, more pronounced AMR signals were also observed in thicker InSb samples (see Figure S8 in the Supporting Information), which implies that the origin of this W-shaped AMR effect may be associated with the bulk property of the InSb(111) material.[34]

3. Conclusion

This study investigated the nonreciprocal magneto-transport phenomenon induced by the interfacial Rashba SOC in InSb/CdTe heterostructures. The achievement of a large Rashba coefficient, long phase-coherent length, and adjustable Fermi energy together contributed to the remarkable UMR response whose coefficient $\gamma = 0.52$ A^{-1} T^{-1} was well maintained up to room temperature. Furthermore, the systematic angular- and

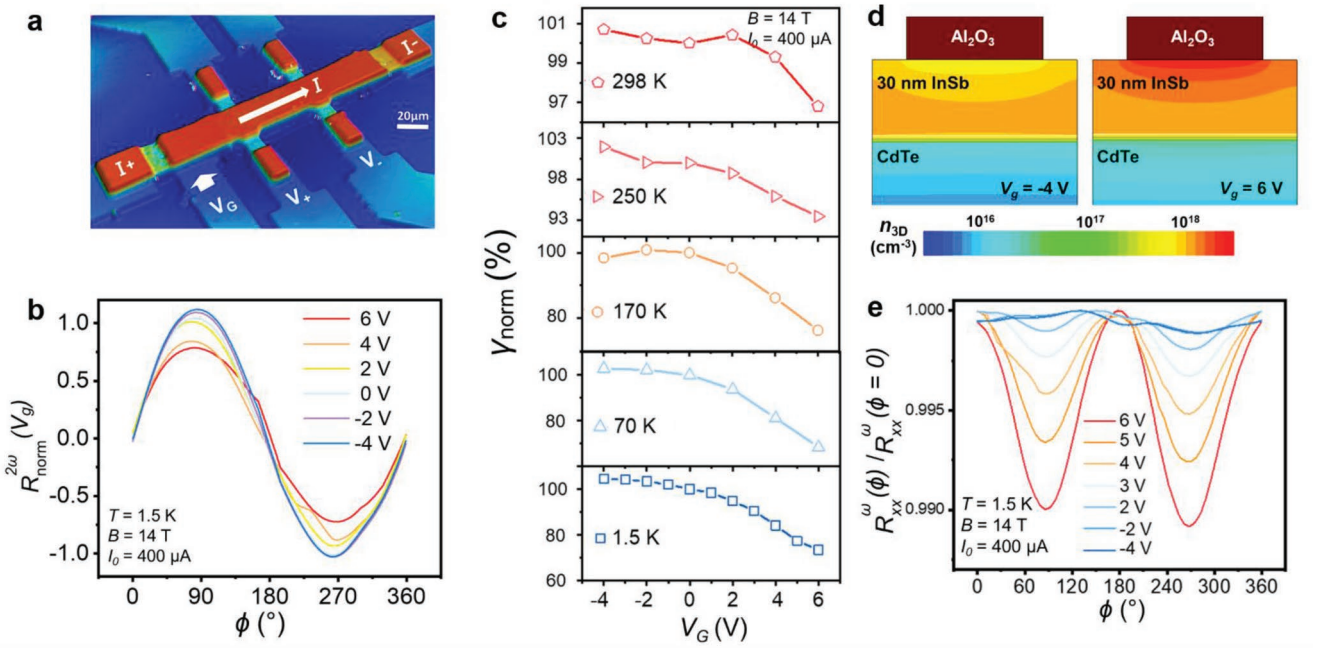

Figure 4. Electric-field control of the first/second-order magnetoresistance strength in the top-gated InSb (30 nm)/CdTe (400 nm) device. a) 3D confocal laser scanning image of the fabricated device with the gate size of 100 μm (length) × 20 μm (width). b) Gate-controlled normalized UMR results of the device by applying the magnetic field within the *xy*-plane at room temperature. c) Electric-field control of the normalized $\gamma_{norm} = \gamma(V_G)/\gamma(V_G = 0\ V)$ at different temperatures varying from 1.5 to 298 K. All γ_{norm} curves follow the same negatively correlated evolution trend with respect to the applied voltage, and the weakened gate tunablity implies the increase of InSb bulk conduction at elevated temperatures. d) TCAD-simulated carrier density distribution profiles in the Al_2O_3/InSb/CdTe trilayer structure at $V_G = -4$ V (left panel) and 6 V (right panel). e) Gate-dependent first-order anisotropic magnetoresistance of the same device. In contrast to the $R^{2\omega}_{norm} - V_G$ behavior, the AMR amplitude gradually increases as V_G changes from –4 to 6 V, reflecting a different mechanism related to the InSb bulk property.

gate-dependent measurements manifested the isotropic spin–momentum locking energy band with an in-plane counter-clockwise spin texture and excelled at salient gate-controlled capability for tuning the UMR (InSb/CdTe heterojunction transport) and AMR (InSb bulk conduction) components. Our results highlight the indispensable role of band engineering in strengthening spin–orbit interactions. Moreover, the lattice-matched material integration concept in narrow-bandgap semiconductor heterostructures may set up a general framework for the design of low-power spin–orbitronics applications (e.g., spin circulators/mixers/isolators over a broad range of frequencies and two-terminal magnetic memory devices) at room temperature.

4. Experimental Section

Sample Growth and Structural Characterization: The InSb/CdTe heterostructure growth was conducted in an ultrahigh-vacuum DCA dual-chamber MBE system with a base pressure of 3×10^{-11} Torr. Semi-insulating ($\rho > 10^6\ \Omega$ cm) 3 in. GaAs (111)B wafers were preannealed in a growth chamber up to 570 °C in a Te-protected environment to remove the native oxide. Subsequently, a two-step growth procedure was adopted for the CdTe growth with a relatively low growth rate of 1.1 Å s^{-1} to obtain a smooth surface morphology. Following moderate postannealing at 355 °C, the CdTe film was exchanged onto another substrate holder and later transferred to the III–V chamber. For the subsequent InSb layer growth, the substrate temperature was maintained at 300 °C, and the growth rate was fixed at 3.5 Å s^{-1}. During epitaxial growth, a beam flux monitor was used to calibrate the element flux rate, and in situ reflection high-energy electron diffraction (RHEED) was applied to monitor the real-time growth conditions. Following the sample growth, atomic force microscopy (AFM) was performed to observe the surface morphology of the as-grown InSb/CdTe sample. In addition, high-resolution scanning transmission electron microscopy (HRSTEM) and electron holography were applied to check the crystal quality and quantify the internal electric-field distribution profile.

Device Fabrication: A 3 in. InSb/CdTe wafer was patterned into a set of micrometer-sized six-terminal Hall bar devices with different crystal orientations using conventional photolithography and ion-beam etching methods. Ti/Au (50 nm/250 nm) was deposited via *e*-beam evaporation to form Ohmic contacts after etching. Further, for the top-gated InSb/CdTe device, a 50 nm thick high-κ Al_2O_3 dielectric layer was deposited by atomic layer deposition (ALD) at 150 °C, and the contact metals were made of Ti/Au/Pt (10 nm/240 nm/50 nm).

Magneto-Transport Measurement: Magneto-transport measurements on both the InSb/CdTe Hall bar and top-gate devices were performed in a He-4 refrigerator (Oxford TeslatronPT system). AC currents with different frequencies and amplitudes during the measurements were applied to the devices using a Keithley 6221 source meter. Subsequently, the first and second harmonic voltages were measured via SR830 lock-in amplifiers, while several experimental variables such as temperature, magnetic field, and rotation angle were varied during the measurements.

Device Simulation: A Sentaurus TCAD device simulator from Synopsys was used to investigate the band diagram and carrier density profile of the top-gated InSb/CdTe device. A typical Al_2O_3 (50 nm)/InSb (30 nm)/CdTe (400 nm) metal–oxide–semiconductor (MOS) structure was defined using SDE tools in Sentaurus Structure Editor. The dielectric constant of Al_2O_3 was set to 8.6 considering the capacitance test result of the ALD-grown Al_2O_3 thin film. During the simulation process, the gate electrode was placed at the top of the Al_2O_3 layer, and the ground electrodes were placed at the right and left edges of the

InSb channel. The designed device structure was later exported to the Sdevice tool, wherein the 2D Poisson solver (including both electrons and holes) was used to obtain the real-space band diagram and carrier distribution under different gate-voltage biases.

Supporting Information

Supporting Information is available from the Wiley Online Library or from the author.

Acknowledgements

This work was sponsored by the National Key R&D Program of China under contract number 2021YFA0715503, the National Natural Science Foundation of China (Grant Nos. 61874172 and 92164104), the Major Project of Shanghai Municipal Science and Technology (Grant No. 2018SHZDZX02), the Shanghai Engineering Research Center of Energy Efficient and Custom AI IC, and the Shanghaitech Quantum Device and Soft Matter Nano-fabrication Labs (SMN180827). X.F.K. acknowledges the support from the Merck POC program and the Shanghai Rising-Star program (Grant No. 21QA1406000). Y.M.Y. acknowledges the support from the Shanghai Pujiang Program (Grant No. 20PJ1411500).

Conflict of Interest

The authors declare no conflict of interest.

Author Contributions

L.L., Y.W., X.L., and J.L. contributed equally to this work. X.F.K. and R.C.C. conceived and supervised this study. H.Z.R., Y.C.J., and C.J.T. prepared the samples. L.L., X.Y. L., J.M.L., and P.Y.H. performed the device fabrication and conducted the transport measurements. Y.Y.W. performed the microscopy characterization. L.L., X.Y.L., J.M.L., and Y.M.Y. analyzed the transport data. Z.H.Z. and Y.Z. conducted the TCAD simulations. L.L., X.Y.L., and X.F.K. wrote the manuscript. All the authors discussed the results and commented on the manuscript.

Data Availability Statement

The data that support the findings of this study are available from the corresponding author upon reasonable request.

Keywords

electric-field control, interfacial Rashba effect, narrow-bandgap semiconductor heterostructures, nonreciprocal transport, spin–orbit coupling

Received: August 11, 2022
Revised: October 30, 2022
Published online:

[1] S. Coleman, *Aspects of Symmetry: Selected Erice Lectures*, Cambridge University Press, Cambridge, UK **1988**.
[2] R. Wakatsuki, N. Nagaosa, *Phys. Rev. Lett.* **2018**, *121*, 026601.
[3] Y. Tokura, N. Nagaosa, *Nat. Commun.* **2018**, *9*, 3740.
[4] D. Choe, M.-J. Jin, S.-I. Kim, H.-J. Choi, J. Jo, I. Oh, J. Park, H. Jin, H. C. Koo, B.-C. Min, S. Hong, H.-W. Lee, S.-H. Baek, J.-W. Yoo, *Nat. Commun.* **2019**, *10*, 4510.
[5] T. Ideue, K. Hamamoto, S. Koshikawa, M. Ezawa, S. Shimizu, Y. Kaneko, Y. Tokura, N. Nagaosa, Y. Iwasa, *Nat. Phys.* **2017**, *13*, 578.
[6] B. Kim, P. Kim, W. Jung, Y. Kim, Y. Koh, W. Kyung, J. Park, M. Matsunami, S.-i. Kimura, J. S. Kim, J. H. Han, C. Kim, *Phys. Rev. B* **2013**, *88*, 205408.
[7] S. R. Park, C. Kim, *J. Electron Spectrosc. Relat. Phenom.* **2015**, *201*, 6.
[8] A. Manchon, H. C. Koo, J. Nitta, S. Frolov, R. Duine, *Nat. Mater.* **2015**, *14*, 871.
[9] R. Winkler, *Phys. Rev. B* **2000**, *62*, 4245.
[10] F. Mireles, G. Kirczenow, *Phys. Rev. B* **2001**, *64*, 024426.
[11] J. Nitta, T. Koga, *J. Supercond.* **2003**, *16*, 689.
[12] P. He, S. S.-L. Zhang, D. Zhu, S. Shi, O. G. Heinonen, G. Vignale, H. Yang, *Phys. Rev. Lett.* **2019**, *123*, 016801.
[13] K. Yasuda, H. Yasuda, T. Liang, R. Yoshimi, A. Tsukazaki, K. S. Takahashi, N. Nagaosa, M. Kawasaki, Y. Tokura, *Nat. Commun.* **2019**, *10*, 2734.
[14] Y. Fu, J. Li, J. Papin, P. Noël, S. Teresi, M. Cosset-Chéneau, C. Grezes, T. Guillet, C. Thomas, Y. Niquet, P. Ballet, T. Meunier, J. Attané, A. Fert, L. Vila, *Nano Lett.* **2022**, *22*, 7867.
[15] a) T. Guillet, A. Marty, C. Vergnaud, M. Jamet, C. Zucchetti, G. Isella, Q. Barbedienne, H. Jaffres, N. Reyren, J.-M. George, A. Fert, *Phys. Rev. B* **2021**, *103*, 064411; b) A. Dyrdał, J. Barnaś, A. Fert, *Phys. Rev. Lett.* **2020**, *124*, 046802.
[16] G. Rikken, J. Fölling, P. Wyder, *Phys. Rev. Lett.* **2001**, *87*, 236602.
[17] P. He, S. S.-L. Zhang, D. Zhu, Y. Liu, Y. Wang, J. Yu, G. Vignale, H. Yang, *Nat. Phys.* **2018**, *14*, 495.
[18] P. He, C.-H. Hsu, S. Shi, K. Cai, J. Wang, Q. Wang, G. Eda, H. Lin, V. M. Pereira, H. Yang, *Nat. Commun.* **2019**, *10*, 1290.
[19] Y. Li, Y. Li, P. Li, B. Fang, X. Yang, Y. Wen, D. Zheng, C. Zhang, X. He, A. Manchon, Z. Cheng, X. Zhang, *Nat. Commun.* **2021**, *12*, 540.
[20] F. Calavalle, M. Suárez-Rodríguez, B. Martín-García, A. Johansson, D. C. Vaz, H. Yang, I. V. Maznichenko, S. Ostanin, A. Mateo-Alonso, A. Chuvilin, I. Mertig, M. Gobbi, F. Casanova, L. E. Hueso, *Nat. Mater.* **2020**, *4*, 071001.
[21] T. Guillet, C. Zucchetti, Q. Barbedienne, A. Marty, G. Isella, L. Cagnon, C. Vergnaud, H. Jaffrès, N. Reyren, J.-M. George, A. Fert, M. Jamet, *Phys. Rev. Lett.* **2020**, *124*, 027201.
[22] J. Li, C. Tang, P. Du, Y. Jiang, Y. Zhang, X. Zhao, Q. Gong, X. Kou, *Appl. Phys. Lett.* **2020**, *116*, 122102.
[23] H. Lichte, M. Lehmann, *Rep. Prog. Phys.* **2007**, *71*, 016102.
[24] Y. Zhao, L. Liu, H. Bi, X. Han, X. Zhao, H. Ni, Y. Xu, Z. Niu, R. Che, *Nanoscale* **2017**, *9*, 11833.
[25] Y. Zhang, F. Xue, C. Tang, J. Li, L. Liao, L. Li, X. Liu, Y. Yang, C. Song, X. Kou, *ACS Nano* **2020**, *14*, 17396.
[26] F. Xue, Y. Zhang, Y. Zhang, L. Liao, L. Li, H. Ruan, L. Sun, J. Dong, C. Tang, G. Yu, Y. Yang, X. Kou, in *2021 IEEE Int. Electron Devices Meeting (IEDM)*, IEEE, Piscataway, NJ, USA **2021**, https://doi.org/10.1109/IEDM19574.2021.9720593.
[27] Q. Liu, X. Zhang, L. Abdalla, A. Zunger, *Adv. Funct. Mater.* **2016**, *26*, 3259.
[28] L. Śniadower, J. Raułuszkiewicz, R. Gałązka, *Phys. Status Solidi B* **1964**, *6*, 549.
[29] A. Tadjine, Y.-M. Niquet, C. Delerue, *Phys. Rev. B* **2017**, *95*, 235437.
[30] G. Bemski, *Phys. Rev. Lett.* **1960**, *4*, 62; b) R. Isaacson, *Phys. Rev.* **1968**, *169*, 312.
[31] P. He, S. M. Walker, S. S.-L. Zhang, F. Y. Bruno, M. Bahramy, J. M. Lee, R. Ramaswamy, K. Cai, O. Heinonen, G. Vignale, F. Baumberger, H. Yang, *Phys. Rev. Lett.* **2018**, *120*, 266802.
[32] G. Rikken, C. Strohm, P. Wyder, *Phys. Rev. Lett.* **2002**, *89*, 133005.
[33] G. Rikken, P. Wyder, *Phys. Rev. Lett.* **2005**, *94*, 016601.
[34] R. Mani, L. Ghenim, J. Choi, *Phys. Rev. B* **1991**, *43*, 12630.